Research Article

Nano Research
2022, 15(4): 3178–3186

ISSN 1998-0124 CN 11-5974/O4
https://doi.org/10.1007/s12274-021-3890-1

Hierarchical yolk-shell structured Li-rich cathode boosting cycling and voltage stabled LIBs

Yanchen Liu[1,2,§], Yafen Chen[1,§], Jing Wang[1], Wei Wang[1], Zhiyu Ding[1], Leyuan Li[1], Yang Zhang[1], Yida Deng[2,3], Junwei Wu[1] (✉), and Yanan Chen[2] (✉)

[1] *Shenzhen Key Laboratory of Advanced Materials, Department of Materials Science and Engineering, Harbin Institute of Technology (Shenzhen), Shenzhen 518055, China*

[2] *School of Materials Science and Engineering, Key Laboratory of Advanced Ceramics and Machining Technology of Ministry of Education, Tianjin Key Laboratory of Composite and Functional Materials, Tianjin University, Tianjin 300072, China*

[3] *School of Materials Science and Engineering, Hainan University, Haikou 570228, China*

[§] *Yanchen Liu and Yafen Chen contributed equally to this work.*

Received: 30 June 2021 / **Revised:** 20 August 2021 / **Accepted:** 15 September 2021

ABSTRACT

Despite the high energy density of lithium-rich (Li-rich) cathodes, their implementation is hampered by the unsatisfied rate capacity and poor cycling performance accompanied with substantial voltage decay. To address these issues, the hierarchical yolk-shell structured $Li_{1.2}Mn_{0.54}Ni_{0.13}Co_{0.13}O_2$ cathodes (YK-LMNCO) was proposed and synthesized through a facile glycerol assisted solvothermal approach and the following lithiation process. Benefitting from the shortened lithium diffusion lengths and the enhanced tolerance to the large volume variation upon lithium ions intercalation/de-intercalation, the unique structure reciprocates an initial coulombic efficiency of 85.8%, an outstanding capacity retention rate of 89.1% after cycling at 2.0 C for 200 cycles with a minor voltage drop, and a capacity retention rate of 93.8% after cycling at 10.0 C for 500 cycles, 85.2% for 1,000 cycles. When assembled with graphite as anode, the YK-LMNCO//graphite full cell shows a remarkable capacity retention rate of 87.2% after cycling at 5.0 C for 50 cycles. Our facile strategy for constructing the yolk-shell structured Li-rich cathodes with high capacity and voltage stability sheds light on synthesizing other lithium storage materials.

KEYWORDS

lithium-rich (Li-rich) layered oxides, yolk-shell structure, cathode, cycling stability, lithium-ion battery (LIBs)

1 Introduction

With the rapid development of electric vehicles (EVs), the requirements for the electrochemical performance of lithium-ion batteries (LIBs) are raising [1]. The electrochemical properties of LIBs depend greatly on the electrode material of the battery, especially the cathode material [2, 3]. However, the current commercialized cathodes, such as $LiCoO_2$ (LCO), $LiNi_{0.80}Co_{0.15}Al_{0.05}O_2$ (NCA), $LiNi_xCo_zMn_yO_2$ (NCM), and $LiFePO_4$ (LFP), still face the challenges of limited cycle life, undesirable specific capacity, and high cost [4–6]. Compared with the commercialized cathodes, Li-rich cathodes $xLi_2MnO_3 \cdot (1-x)LiMO_2$ (M = Mn, Ni, Co) can be charged exceed 4.5 V, enabling a high specific capacity over 250 mAh/g [3, 7]. Besides, Li-rich cathodes also take advantages of low cost and toxicity, thus enter the spotlight of the cathodes for next-generation power batteries. However, the inferior rate capability and the poor cycling stability still need to be solved prior to commercial application [8, 9].

To optimize the above issues, various hierarchical structure has been put forward to simultaneously enhance the bulk lithium diffusion kinetics and maintain the framework stability [10–15]. Among them, nano particles assembled solid nano/microspheres have been widely applied owing to the advantages of high energy density. However, the secondary solid aggregates tend to be fragile as a result of the accumulated interior stress and strain upon prolonged cycling, leading to the structure failure and poor cycling stability [16–18]. Compared with the solid nano/microspheres, the hollow space of yolk-shell nano/microspheres can buffer the volume change and reduce the mechanical strain during cycling, leading to the enhanced structure stability than that of solid nano/microspheres structure [14, 19]. Additionally, the internal cavity in yolk-shell structure could further reduce Li^+ diffusion distance and provide additional reaction sites for Li^+ storage, resulting in the improved rate capability [20, 21].

Until now, while the preparation of nano-type yolk-shell structure is frequently reported for the metal oxides of anode materials, the synthesis of micro-type yolk-shell structure still faces with challenges, especially for cathodes which own more complex chemical compositions and need higher calcination temperature than those of anodes. To address the issue above, template method, such as taking MnO_2 as self-template, was adopted for the synthesis of yolk-shell nano/micro structured cathodes. However, the template method undoubtedly increases the preparation complexity and losses the atomic-level uniform mixing of transition metals [22]. Therefore, synthesizing Li-rich

Address correspondence to Junwei Wu, junwei.wu@hit.edu.cn; Yanan Chen, yananchen@tju.edu.cn

cathodes with yolk-shell structure by a facile, MnO_2 template-free strategy is still a challenge.

Herein, a facile template-free solvothermal approach and the following calcination process were proposed to fabricate hierarchical yolk-shell structured Li-rich cathodes. By adjusting the molar concentration of transition metal salt, spherical precursors with different diameters were obtained. Among them, the as-prepared yolk-shell structured $Li_{1.2}Mn_{0.54}Ni_{0.13}Co_{0.13}O_2$ cathodes with diameter of 1.3–1.5 μm (YK-LMNCO) demonstrated the best electrochemical performance. Besides, in comparison of the as-prepared solid microspheres structured $Li_{1.2}Mn_{0.54}Ni_{0.13}Co_{0.13}O_2$ cathodes (SM-LMNCO), YK-LMNCO showed much improved electrochemical performance, including an initial coulombic efficiency of 85.8%, a high capacity of 156.5 and 122.7 mAh/g at 5.0 and 10.0 C, respectively, and an outstanding capacity retention rate of 93.8% after cycling at 10.0 C for 500 cycles. At the same time, the voltage drop was also significantly reduced in the YK-LMNCO. When taking graphite as anode, the full cell demonstrated a capacity retention rate of 87.2% at 5.0 C for 50 cycles. Such superior electrochemical performance of YK-LMNCO is ascribed to the synergistic effect of the reduced Li^+ diffusion length, the reinforced micro-framework, and the restricted phase transition.

2 Results and discussion

2.1 Morphology and structure characterizations

The schematic diagram for the synthesis of LMNCO with yolk-shell structure was illustrated in Fig. 1. Under solvothermal conditions at 180 °C, isopropanol and NO_3^- underwent redox reactions and formed OH^-, which combined with the transition metal ions and led to the formation of transition metal hydroxide [19]. Meanwhile, glycerol molecules acted as the soft template for the growth of transition metal hydroxide by self-assembling into a quasi-emulsion of isopropanol through strong molecular hydrogen bonding, preventing the aggregation of transition metal hydroxide via the templating effect and leading to the formation of uniform spheres structured precursors [19]. The scanning electron microscope (SEM) images of precursors without and with the addition of glycerol in the experiment were shown in Fig. S1 in the Electronic Supplementary Material (ESM). Obviously, the absence of glycerol (glycerol was replaced with an equal amount of isopropanol) led to the formation of precursors with irregular shape (Figs. S1(a) and S1(b) in the ESM) instead of uniform microspheres structure (Figs. S1(c) and S1(d) in the ESM). In addition to the morphology, the adding of glycerol also affected the phase structure of precursors, resulting in the formation of transition metal (TM) hydroxide-glycerol composites (which is a kind of metal alkoxides) [19, 23]. By adjusting the molar concentration of transition metal salt, the precursors with various diameter were obtained, as shown in the Fig. S2 in the ESM. The SEM and transmission electron microscopy (TEM) results of the precursors of YK-LMNCO were shown in Fig. 2(a) and inset, which showed well-dispersed uniform solid microspheres with a diameter of 1.3–1.5 μm. Upon calcining at 500 °C for 6 h in air, the solid microspheres structured precursors were converted to yolk-shell structured transition metal oxides with an internal cavity formed between the core and shell, as shown in Fig. 2(b) and inset. Additionally, the surface of transition metal oxide became rougher than that of the precursors. Energy dispersive X-ray spectroscopy (EDS) and inductively coupled plasma (ICP) (Figs. 2(d) and 2(e), Table S1 in the ESM) results showed the atomic ratio of Mn: Ni: Co was very close to the designed value of 0.54:0.13:0.13. Moreover, the elemental mappings (Figs. 2(i)–2(m)) revealed the existence and uniform distribution of Ni, Co, Mn, and O in the core and shell without elemental enrichment and segregation.

The formation of the yolk-shell structured transition metal oxides was mainly ascribed to the comprehensive effect of contraction of the core and adhesion of the shell caused by the non-equilibrium heat treatment process, as shown in Fig. S3 in the ESM [24, 25]. Specifically, during the initial annealing process, the large temperature gradient along the radial direction led to the rapid forming of the transition metal oxides thin shell on the surface of the metal alkoxides microspheres [24]. Thereafter, there were two actions in opposing directions existing on the interface between the transition metal oxides shell and the metal alkoxides core. One was the inward contraction (F_c) of the metal alkoxides organic species due to the weight loss caused by its oxidative degradation, as confirmed by the thermal gravity analysis (TGA) result in Fig. 3(b), resulting in inward shrinkage of the core. The other was the adhesion action (F_a) from the pre-formed relatively rigid shell, which prohibited the inward shrinkage. As the annealing process went on, F_c became dominant, causing the

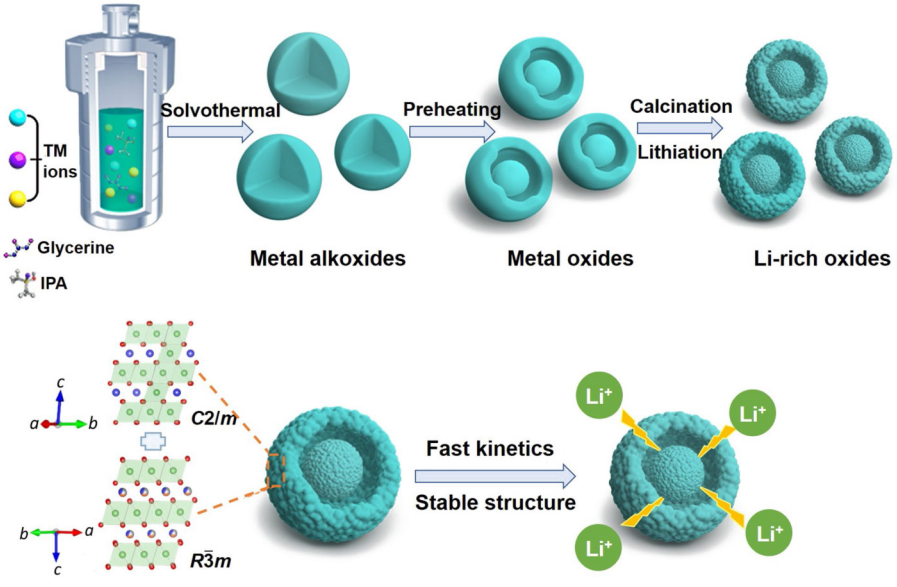

Figure 1 Schematic illustration for the synthesis of yolk-shell structured Li-rich cathodes.

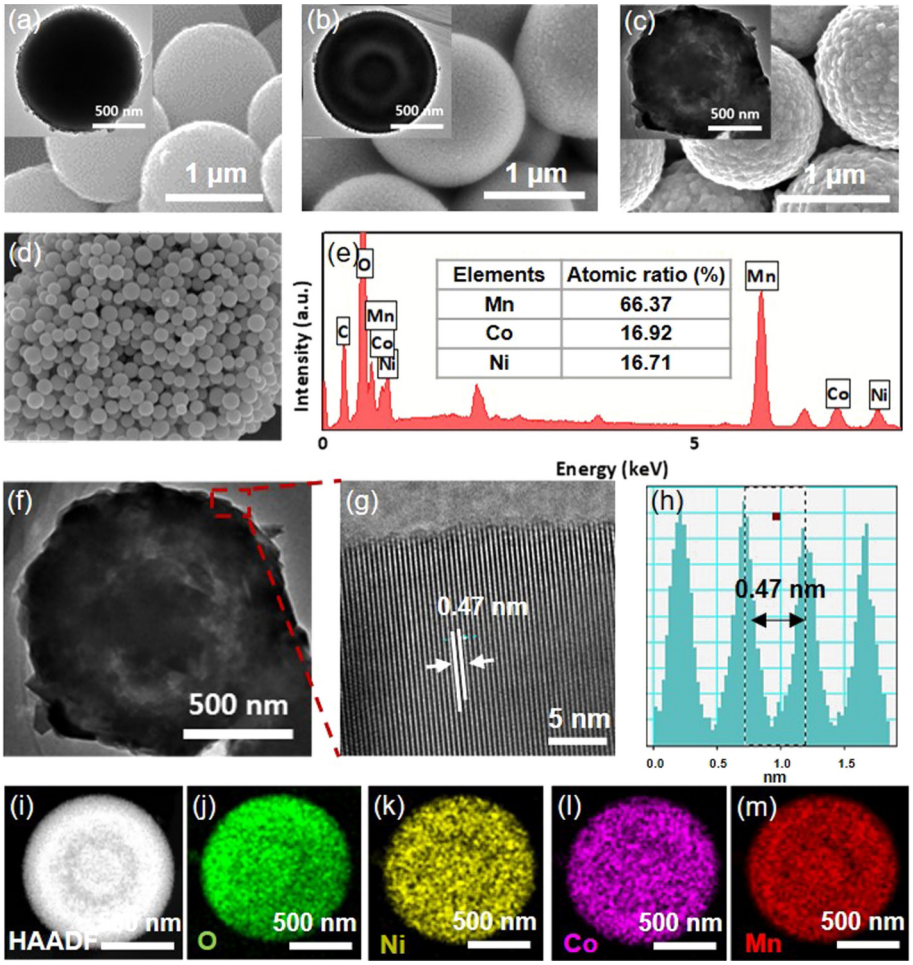

Figure 2 SEM images of (a) precursor spheres; (b) transition metal oxides; and (c) YK-LMNCO, respectively, inset: the corresponding TEM images; (d) and (e) EDS results of transition metal oxides; (f) TEM image of YK-LMNCO; (g) HRTEM image of the selected region in (f), (h) linear analysis of zones for (g); (i)–(m) elemental mappings of the yolk-shell structured transition metal oxides.

inner core further contracted inward and separates from the outer metal oxides shell. With prolonged thermal treatment, the heterogeneous contraction process took place, leading to the formation of yolk-shell structured transition metal oxides.

The influence of the heating rate on the formation process of yolk-shell structure was also investigated. The transition metal oxides obtained by annealed the metal alkoxides at the heating rate of 1, 5, and 10 °C/min were shown in Fig. 2(b) and Fig. S4 in the ESM. In comparison with transition metal oxides with a slow heating rate of 1 °C/min, the increasing of heating rate visibly decreased the thickness of the shell. Specifically, as shown in Fig. 2(b) inset, yolk-shell structure with the shell thickness of 200–300 nm was obtained with a heating rate of 1 °C/min. At a higher heating rate of 5 °C/min, the accessed transition metal oxides still showed a yolk-shell structure (Fig. S4(a) in the ESM), but the shell thickness decreased to 100–200 nm. Further increasing the heating rate to 10 °C/min, the shell thickness decreased to only 20–50 nm (Fig. S4(b) in the ESM). Such phenomenon was also observed in Lou's work [24]. The thin shell obtained at the higher heating rate was very fragile and easily broke or even fell away from the core after further annealing at 800 °C for 15 h, as shown in Fig. S5 in the ESM. Besides, fast heating rate also reduces the crystallinity of the materials. Accordingly, the slow heating rate of 1 °C/min was chosen to obtain the transition metal oxides.

Followed by the lithiation of transition metal oxide and further calcination at 800 °C for 15 h, the Li-rich cathodes was obtained. As shown in Fig. 2(c) and inset, the yolk-shell structure was well maintained in the as-prepared YK-LMNCO cathodes with a heating rate of 1 °C/min. The larger range of SEM image of the YK-LMNCO was also shown in Fig. S6 in the ESM. Notably, the core and shell of YK-LMNCO were both assembled by the detectable crystalline nanoparticles with a length of ~ 80 nm. Thus YK-LMNCO not only inherits the merit of yolk-shell (YK) structure, but also owns the advantage of hierarchical nano/microsphere structure including the relatively high volumetric energy density of microspheres and the shortened Li^+ transport pathways from primary nanoparticles [26, 27].

TEM image (Fig. 2(c) inset) showed that YK-LMNCO possessed an inner solid core with diameter of 300–400 nm and an outer shell with thickness of 200–300 nm. The internal void between the core and shell in the yolk-shell structure is expected to provide more sites for Li^+ storage and buffer the structural strain during charging and discharging [28]. To further confirm the crystal structure of YK-LMNCO, high-resolution transmission electron microscopy (HRTEM) results of the selected region of Fig. 2(f) were shown in Fig. 2(g). Combined HRTEM and its linear analysis of zones (Fig. 2(h)), the apparent interlayer space of 0.47 nm was observed and can be identified to the (003) plane of the $LiMO_2$ hexagonal phase and (001) plane of the Li_2MnO_3 monoclinic phase [29, 30].

For comparison, the solid nano/microsphere structured LMNCO (SM-LMNCO) was also synthesized, as shown in Fig. S7 in the ESM. The TEM image (Fig. S7(f) in the ESM) validated the solid structure of SM-LMNCO, HRTEM image confirmed the layered phase of SM-LMNCO (Fig. S7(g) in the ESM), and the ICP results demonstrated the SM-LMNCO with designed atomic ratio (Table S1 in the ESM).

The N_2 physisorption isotherms recorded for SM-LMNCO and YK-LMNCO were shown in Fig. S8 in the ESM. The Brunauer–Emmett–Teller (BET) surface area of SM-LMNCO and YK-LMNCO were 1.49 and 4.82 m^2/g, respectively. The BET specific surface area of YK-LMNCO was about three times that of SM-LMNCO, owing to the unique yolk-shell structure. In addition, the total pore volume of YK-LMNCO was 2.47×10^{-2} cm^3/g, much larger than that of SM-LMNCO (1.21×10^{-2} cm^3/g). Thus, the higher surface area and pore volume of YK-LMNCO can offer more reaction sites for lithium storage, which is favorable for enhancing lithium diffusion kinetics [28].

The X-Ray diffraction (XRD) pattern of the precursors for YK-LMNCO was depicted in the lower curve of Fig. 3(a). There is an obvious diffraction peak at ~ 10°, representing the characteristic peak of metal alkoxides [24, 25]. Figure 3(b) showed the TGA result of the metal alkoxides. The significant weight loss of ~ 46.5% was mainly triggered by the oxidative degradation of the organic species, leading to the inward shrinkage of the core [31]. Besides, there was almost no weight loss anymore when the sintering temperature exceed 500 °C. This explains why 500 °C was chosen as the preheating temperature to obtain corresponding metal oxides. The XRD pattern of the transition metal oxide was shown in the upper curve of Fig. 3(a). All of the diffraction peaks can be matched to $NiMn_2O_4$ with spinel-like structure. The XRD patterns of the as-prepared YK-LMNCO and SM-LMNCO were identified in Fig. 3(c) and Fig. S9 in the ESM, respectively. It can be found that all the dominant diffraction peaks can be well indexed to the hexagonal $LiMO_2$ (space group: $R\bar{3}m$) and several weak diffraction peaks between 20° and 25° are consistent with the monoclinic Li_2MnO_3 (space group: $C2/m$) [32]. No impurity peaks can be found in the XRD pattern, demonstrating the high purity of the as-prepared YK-LMNCO and SM-LMNCO. The X-ray photoelectron spectroscopy (XPS) spectra were presented to probe the valence state of YK-LMNCO on the surface (Figs. 3(d)–3(f)). All the spectra were calibrated using the binding energy of C 1s (284.6 eV). The Co $2p_{3/2}$ at ~ 780.0 eV with satellite peak at ~ 789.5 eV is ascribed to Co^{3+} (Fig. 3(d)) [33], the Ni $2p_{3/2}$ at ~ 854.9 eV with a satellite peak at ~ 861.5 eV reflects the main valence state of Ni is +2 (Fig. 3(e)) [12], the Mn $2p_{3/2}$ (642.6 eV) can be fitted to the Mn^{4+} (Fig. 3(f)) [34].

In sum, all the characterization above confirmed the formation of YK-LMNCO with desired yolk-shell structured framework, well-ordered layered structure, and chemical composition. Thus, an enhanced electrochemical performance can be expected for YK-LMNCO.

2.2 Electrochemical properties

The electrochemical properties were evaluated in Li//LMNCO half cells at the voltage range of 2.0–4.8 V. The cycle performance of LMNCO adopting different molar concentration of transition metal salt were shown in Fig. S10 in the ESM, and the results highlighted the importance of synthesizing yolk-shell structure with appropriate diameter of 1.3–1.5 μm. The initial charge/discharge profiles of SM-LMNCO and YK-LMNCO at 0.1 C (1 C = 200 mA/g) were shown in Fig. 4(a). Both samples delivered the typical voltage profiles of Li-rich cathodes including a sloping region < 4.45 V (the extraction of Li^+ from the $LiMO_2$ component) and a plateau region at 4.45 V (the extraction Li^+ and oxygen from the Li_2MnO_3 component) [35]. The initial charge and discharge capacity of SM-LMNCO were 328.1 and 266.8 mAh/g, corresponding to an initial coulombic efficiency of 81.3%. By comparison, YK-LMNCO showed a relatively high initial coulombic efficiency of 85.8% with a discharge capacity of 274.5 mAh/g. The higher initial coulombic efficiency of YK-LMNCO may result from the enhanced lithium intercalation kinetics during discharging process [36].

The cycling and voltage stability of SM-LMNCO and YK-LMNCO were compared in Fig. 4(b). Followed by cycling at 2.0 C for 200 cycles, the YK-LMNCO retains a discharge capacity of 163.8 mAh/g with a capacity retention of 89.1%, much higher than discharge capacity of 134.1 mAh/g with capacity retention of 79.5% for SM-LMNCO. Such result reflected the importance of constructing the yolk-shell structure, which can enable a superior cycling stability. In addition, focus should be paid on the voltage stability of YK-LMNCO, as the voltage decay occurred simultaneously with the loss of the energy density for the cell. As shown in Fig. 4(b) inset, a voltage decay of only 0.12 V within 100 cycles was demonstrated for the YK-LMNCO, which was comparable or smaller to the reported work (Table S2 in the ESM). Besides, the voltage profiles in Fig. 4(c) and differential capacity versus voltage (dQ/dV) plots in Fig. 4(c) inset further confirmed the slight voltage decay of YK-LMNCO. The enhanced voltage retention reflected the reduced phase transition and the well-maintained layered structure of YK-LMNCO [9].

Figure 4(d) illustrated the rate performance of SM-LMNCO and YK-LMNCO. SM-LMNCO demonstrated a relatively low

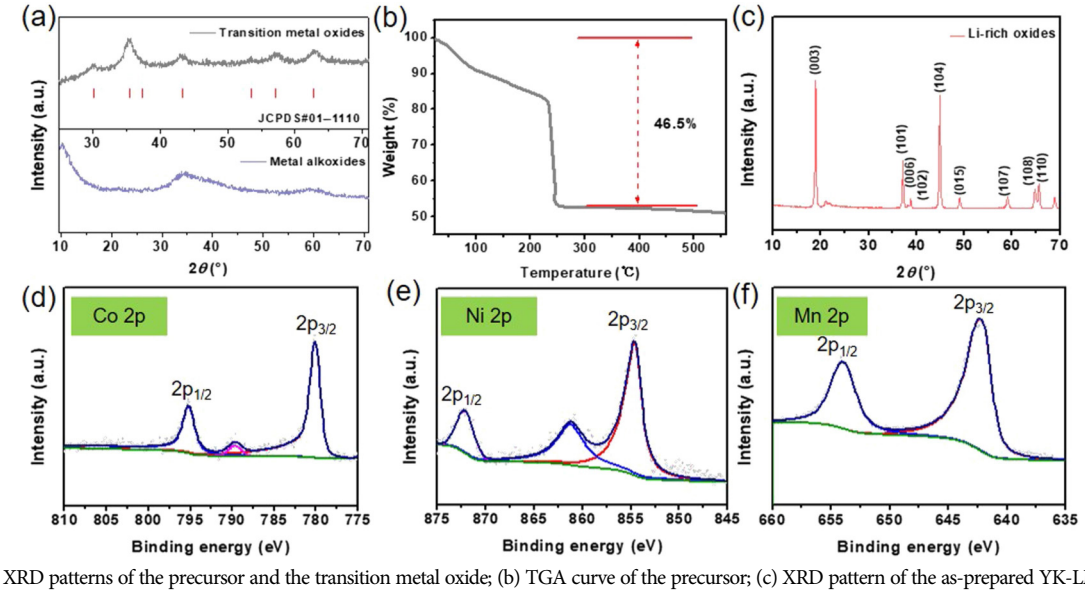

Figure 3 (a) XRD patterns of the precursor and the transition metal oxide; (b) TGA curve of the precursor; (c) XRD pattern of the as-prepared YK-LMNCO; (d)–(f) the typical XPS spectra for Co 2p, Ni 2p, and Mn 2p of YK-LMNCO, respectively.

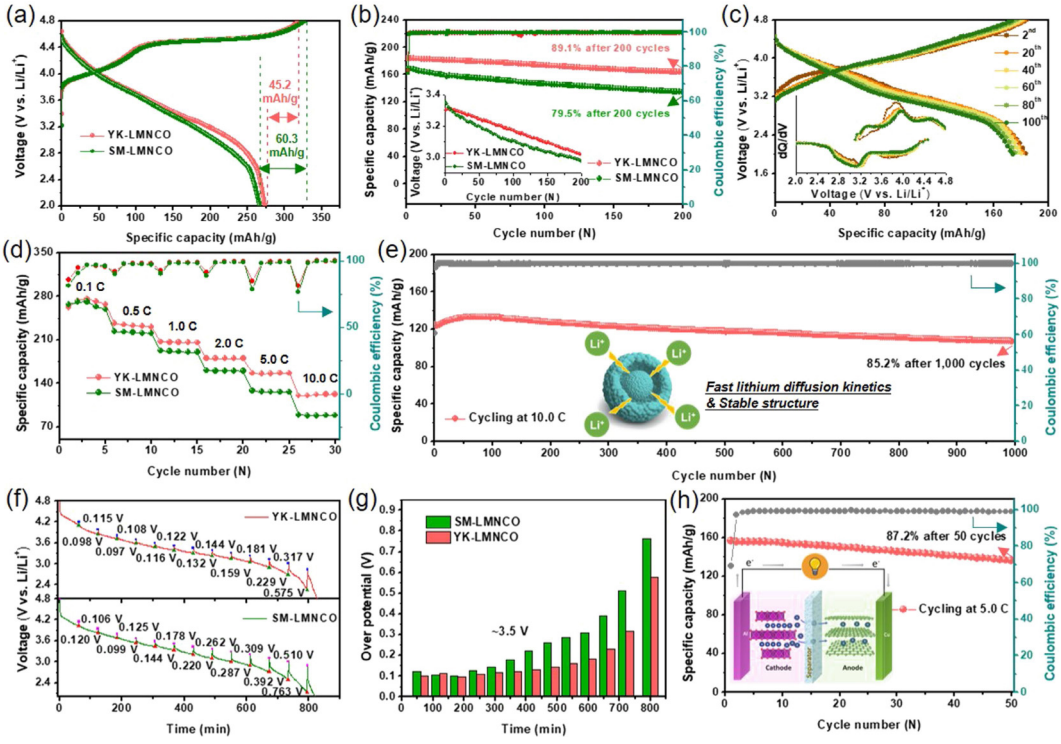

Figure 4 (a) The initial charge/discharge profiles of SM-LMNCO and YK-LMNCO at 0.1 C (1 C = 200 mA/g); (b) cycle performances of SM-LMNCO and YK-LMNCO at 2.0 C, inset: the voltage performance of YK-LMNCO; (c) voltage profiles extracted from the chosen cycles for YK-LMNCO at 2.0 C, inset: the dQ/dV curves of the corresponding cycles; (d) rate capabilities at various rates from 0.1 to 10.0 C of SM-LMNCO and YK-LMNCO; (e) cycling test of YK-LMNCO at 10.0 C; (f) GITT; and (g) over-potential curves of SM-LMNCO and YK-LMNCO during the initial discharging process; (h) the cycle performance of YK-LMNCO//graphite at 5.0 C, inset: schematic diagram of LMNCO//graphite full cell.

specific capacity of 160.9, 127.8, 89.5 mAh/g at 2.0, 5.0, 10.0 C, respectively, while YK-LMNCO delivered a high specific capacity of 180.1, 156.5, 122.7 mAh/g at 2.0, 5.0, 10.0 C, respectively. Remarkably, the rate performance of YK-LMNCO was also comparable with the other reported hollow structured cathode materials [37–40]. The reaction kinetics of SM-LMNCO and YK-LMNCO during the 1st discharge process were evaluated by the galvanostatic intermittent tritration technique (GITT), as shown Fig. 4(f). The voltage variation between the end of each interrupted discharge and the end of relaxation was defined as the over-potentials [41–43]. The larger the over-potentials, the poorer the reaction kinetics [41]. As shown in Fig. 4(g), the over-potentials of both YK-LMNCO and SM-LMNCO increased continuously during the discharging process, especially after 350 min (corresponding to the discharge voltage below ~ 3.5 V). The unsatisfactory Li^+ diffusion kinetics below ~ 3.5 V were relevant to the undesirable lithium intercalation kinetics of the MnO_2 [44]. It is obviously that the over-potentials of YK-LMNCO below ~ 3.5 V were significantly lower than that of SM-LMNCO, demonstrating that YK-LMNCO owned better reaction kinetics than that of SM-LMNCO, in accordance with its better rate performance. To further highlight the rate and cycling stability of YK-LMNCO, the coin-cell was subjected to an ultrahigh rate of 10.0 C for 1,000 cycles (Fig. 4(e)). The YK-LMNCO kept a specific capacity of 117.6 mAh/g after 500 cycles (capacity retention rate of 93.8%), and a specific capacity of 106.9 mAh/g after 1,000 cycles (capacity retention rate of 85.2%). The excellent electrochemical performance of YK-LMNCO makes it possible to be practically used in LIB with high energy/power density. Hence, YK-LMNCO was assembled in full cell employing graphite as anode, as shown in Fig. 4(h) inset. The YK-LMNCO showed excellent capacity retention rate of 87.2%, after cycling at high rate of 5.0 C for 50 cycles (Fig. 4(h)).

The excellent cycling stability and rate capability is inseparable from their unique hierarchical yolk-shell structure. Specifically, the primary nanoparticles in the YK-LMNCO hollow microspheres can offer a short Li^+ transmission route, meanwhile, the empty space could provide additional reaction sites for Li^+ storage, hence enabling fast Li^+ insertion/extraction [45]. Additionally, the unique yolk-shell hollow architecture could mitigate the mechanical strain that caused by volume variation during the repeated Li^+ insertion/extraction, thereby significantly improving the structure integrity [46].

To probe the integrity of the bulk structure which coupled the electrochemical stability of the material, the *ex-situ* SEM characterizations of cycled SM-LMNCO and YK-LMNCO were shown in Figs. 5(b) and 5(c). Obviously, YK-LMNCO demonstrated the well-maintained microsphere structure, as shown in Fig. 5(c). In addition, the internal void still maintains in the cycled YK-LMNCO, as confirmed by the TEM image (Fig. 5(c) inset). Accordingly, the internal cavity in the YK-LMNCO is conductive to release the volume change-induced microstrains, thus endowing the stable structure framework. In contrast, SM-LMNCO showed unwanted cracks and structure fragmentations after cycling, reflecting that the solid structured SM-LMNCO was more easily subject to the accumulated microstrains at the boundaries of closely stacked primary particles [47, 48]. The structure integrity and voltage stability are closely connected, as shown in Fig. 5(a), the cracks of SM-LMNCO led more area exposed to the electrolytes and give rise to new reaction sites for interfacial reactions, facilitating substantial oxygen loss inside the bulk structure, reducing the migration barriers of transition metals, promoting the layered to spinel-like phase transition and leading to severer voltage decay [17, 49–54]. The Raman spectroscopy (Figs. 5(d) and 5(e), and Fig. S11 in the ESM) can focus on the material's general structure and has been validated to be particular sensitive to the variation of metal-oxygen

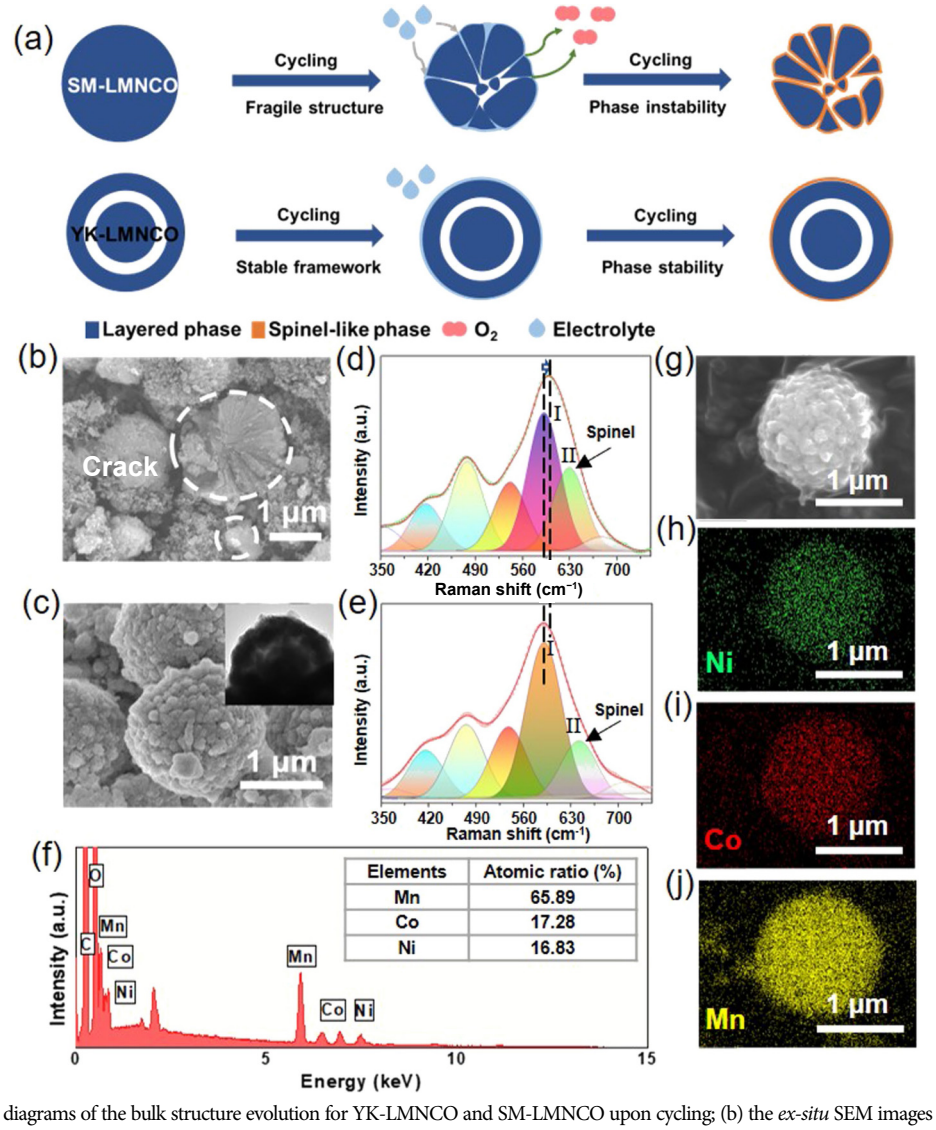

Figure 5 (a) Schematic diagrams of the bulk structure evolution for YK-LMNCO and SM-LMNCO upon cycling; (b) the *ex-situ* SEM images of cycled SM-LMNCO; and (c) YK-LMNCO, respectively, inset: the *ex-situ* TEM image of cycled YK-LMNCO; (d) and (e) the *ex-situ* Raman characterizations of cycled SM-LMNCO and YK-LMNCO, respectively; (f) EDS results of cycled YK-LMNCO; (g)–(j) elemental mappings of cycled YK-LMNCO.

bonds in layered and spinel-like structure [55]. The peak positions at ~ 470 and ~ 599 cm^{-1} can be matched with E_g (O–M–O bending mode) and A_{1g} (the M–O stretching mode) vibrations of $R\bar{3}m$ structure, respectively. The other peak positions at ~ 410 and ~ 520 cm^{-1} are assigned to the phonon vibrations of Li_2MnO_3 [56]. Additionally, the appearance of the peak at ~ 630 cm^{-1} (A_{1g} for the spinel phase) suggests the formation of spinel-like phase [56]. As shown in Figs. 5(d) and 5(e), and Fig. S11 in the ESM, the peak position of the SM-LMNCO at ~ 599 cm^{-1} shifted right significantly after cycling under the influence of the spinel-like phase at ~ 630 cm^{-1} while the peak position of YK-LMNCO at ~ 599 cm^{-1} delivered no obvious changes, evidencing the more severe layered to spinel-like phase transition and voltage attenuation of SM-LMNCO. To better evaluate the degree of phase transition in YK-LMNCO and SM-LMNCO, the Raman results of cycled materials were fitted and the ratio of the peak area of "II" (spinel-like phase) to the peak "I" (layered phase) were calculated. The calculated ratios in YK-LMNCO and SM-LMNCO were 36.9% and 60.1% respectively, demonstrating that the phase transition of YK-LMNCO with a yolk-shell structure was remarkably mitigated than that of SM-LMNCO. It is believed that the continuous phase transition and the triggered anisotropic variation of the lattice parameters are the primary reasons for the voltage drop and bulk degradation [51]. Thus YK-LMNCO with much less spinel-like phase owned a well-maintained layered structure, in accordance with its excellent electrochemical performance above. EDS (Fig. 5(f)) revealed that cycled YK-LMNCO demonstrated a very small deviation in the atomic ratio of transition metals, in comparison with uncycled YK-LMNCO. Elemental mappings confirmed the uniform distribution of Mn, Ni, Co in the cycled YK-LMNCO (Figs. 5(g)–5(j)).

3 Conclusions

In summary, hierarchical yolk-shell structured $Li_{1.2}Mn_{0.54}Ni_{0.13}Co_{0.13}O_2$ cathode materials have been successfully prepared through a facile template-free glycerol assisted solvothermal method and the followed heat treatment. The nano-sized primary particles help to reduce the lithium diffusion path, while the macro-sized secondary microspheres maintain the structure stability. More importantly, comparing with the SM-LMNCO, the interior voids of the YK-LMNCO aids to preserve the integrity of the micro-framework by accommodating the large volume variation. Ascribed to its unique yolk-shell structure and moderate microsphere size, YK-LMNCO delivers a capacity retention rate of 89.1% after 200 cycles at 2.0 C and an outstanding capacity

retention rate of 85.2% after cycling at 10.0 C for 1,000 cycles. The facile template-free method of preparing yolk-shell structure can also be adopted to design other cathode materials for high performance LIBs.

4 Experimental section

4.1 Material preparation

All reagents and solvents were of analytical grade and were used without further purification. In a typical procedure, the molar concentration of transition metal salt was kept at 0.019 mol/L. Specifically, 3.1 mmol of $Mn(NO_3)_2$ (50 wt.% aqueous solution, Aladdin), 0.746 mmol of $Ni(NO_3)_2{\cdot}6H_2O$ (99.0%, Aladdin), and 0.746 mmol of $Co(NO_3)_2{\cdot}6H_2O$ (99.0%, Aladdin), were dissolved into the solvents of 40 mL glycerol (99.0%, Aladdin) and 200 mL isopropanol (99.5%, Aladdin), which was stirred continuously to make a transparent solution. Subsequently, 60 mL of the mixture was placed in a 100 mL Teflon-lined stainless steel autoclave. After kept at 180 °C for 6 h, the precursor was collected by centrifugation and washed with ethanol for several times. The dried precursor was further calcined at 500 °C for 6 h with a heating rate of 1 °C/min to form transition metal oxides ($Mn_{0.675}Ni_{0.1625}Co_{0.1625}O_x$). After mixing the transition metal oxides and Li salts, the mixture was finally calcined at 800 °C for 15 h to perform the YK-LMNCO. The $Li_{1.2}Mn_{0.54}Ni_{0.13}Co_{0.13}O_2$ material with molar concentration of transition metal salt of 4.4 mmol/L, 8.9 mmol/L, 0.033 mol/L and 0.069 mol/L were also synthesized and named as LMNCO-0.44, LMNCO-0.89, LMNCO-3.33, and LMNCO-6.94, respectively.

For comparison, the solid microspheres structured $Li_{1.2}Mn_{0.54}Ni_{0.13}Co_{0.13}O_2$ cathodes (SM-LMNCO) were prepared by solvothermal method using hexamethylenetetramine (HMT) as precipitant. Specifically, 7.5 mmol HMT (99.0%, Aladdin) was dissolved in 35 mL mix solvents of dimethyl formamide (DMF) and deionized (DI) water and continuously to make a transparent solution. After that, 0.813 mmol $C_4H_6CoO_4{\cdot}4H_2O$ (99.0%, Aladdin), 0.813 mmol $C_4H_6NiO_4{\cdot}4H_2O$ (99.5%, Aladdin), and 3.375 mmol $C_4H_6MnO_4{\cdot}4H_2O$ (99.0%, Aladdin) were put in the above solution and stirred for 1 h. The solution was then placed in a 50 mL Teflon-lined stainless steel autoclave. After kept at 160 °C for 24 h, the precipitate was centrifuged, washed with ethanol and distilled water to get the carbonate precursor ($Mn_{0.675}Ni_{0.1625}Co_{0.1625}CO_3$). The precursor was first calcined at 500 °C for 6 h to obtain the transition metal oxide ($Mn_{0.675}Ni_{0.1625}Co_{0.1625}O_x$). The transition metal oxides were mixed with Li salt and then were calcining at 800 °C for 15 h to get the solid microsphere structured LMNCO (SM-LMNCO).

4.2 Material characterization

The crystal structure of the cathode materials was analyzed by XRD (Rigaku D/max 2500 PC system, Cu Kα radiation, 40 kV, 200 mA). The morphological characterization of the cathode materials was obtained by SEM (Hitachi S4700). TEM (JEOL2100F) equipped with EDS was taken to investigate the crystal structure and elemental distribution of the samples. TGA (NETZSCH STA 449F3) was conducted from room temperature to 1,000 °C to monitor the material behavior during annealing. Inductively coupled plasma optical (ICP, MDTC-EQ-M29–01) was used to determine the elemental ratio of the cathode materials. XPS (PHI5600, Perkin Elmer) were used to identify the chemical valence state of the cathode materials. The Raman characterization was investigated using Renishaw invia Reflex spectrometer equipped with microscope in a reflectance mode with a 532 nm laser source. The specific surface area of the samples was determined by the BET method with N_2 physisorption measurement on a surface area (Micromeritics ASAP 2020).

4.3 Electrochemical measurements

CR2032-type coin-cells were assembled in the glovebox with water and oxygen < 0.1 ppm. The assembled coin-cells taking the as-prepared Li-rich materials as cathode, lithium metal as anode, Celgard 2400 as separator. The electrolyte was purchased from Zhangjiagang Guotai Huarong Chemical New Material Co., Ltd. The cathode slurry was composed of Li-rich cathode materials (75 wt.%), Super P (15 wt.%) and polyvinylidene fluoride (PVDF, 10 wt.%) in N-methyl pyrrolidone solvents (NMP). The resulting slurry was coated uniformly on aluminum foil and dried at 110 °C for 12 h under vacuum. A Neware test system was applied to carry out the galvanostatic charge/discharge tests in the voltage range of 2.0 and 4.8 V (vs Li^+/Li). The testing current rates ranged from 0.1 to 10.0 C (1 C = 200 mA/g). The electrochemical impedance spectroscopy (EIS) was analyzed on the Gamry electrochemical workstation with frequencies ranging from 0.01 Hz to 100 kHz.

Acknowledgements

The authors acknowledge the financial support from Natural Science Foundation of Guangdong Province (No. 2018A030313721), the National Key Research and Development Program of China (No. 2018YFB0703500) and the National Natural Science Foundation of China (No. 91963113).

Electronic Supplementary Material: Supplementary material (more physical characterization of YK-LMNCO and SM-LMNCO, cycling performance of yolk-shell structured LMNCO with different diameters) is available in the online verion of this article at https://doi.org/10.1007/s12274-021-3890-1.

References

[1] Cui, B. H.; Hu, Z.; Liu, C.; Liu, S. L.; Chen, F. S.; Hu, S.; Zhang, J. F.; Zhou, W.; Deng, Y. D.; Qin, Z. B. et al. Heterogeneous lamellar-edged Fe-Ni$(OH)_2/Ni_3S_2$ nanoarray for efficient and stable seawater oxidation. *Nano Res.* **2021**, *14*, 1149–1155.

[2] Yang, C.; Lv, F.; Zhang, Y. L.; Wen, J.; Dong, K.; Su, H.; Lai, F. L.; Qian, G. Y.; Wang, W.; Hilger, A. et al. Confined Fe_2VO_4⊂nitrogen-doped carbon nanowires with internal void space for high-rate and ultrastable potassium-ion storage. *Adv. Energy Mater.* **2019**, *9*, 1902674.

[3] Yang, C.; Lv, F.; Dong, K.; Lai, F. L.; Zhao, K. N.; Sun, F.; Dou, S. M.; Wang, Q.; Xu, J.; Zhang, P. P. et al. Carbon-coated ultrathin metallic V_5Se_8 nanosheet for high-energy-density and robust potassium storage. *Energy Storage Mater.* **2021**, *35*, 1–11.

[4] Hou, P. Y.; Zhang, H. Z.; Zi, Z. Y.; Zhang, L. Q.; Xu, X. J. Core-shell and concentration-gradient cathodes prepared via co-precipitation reaction for advanced lithium-ion batteries. *J. Mater. Chem. A* **2017**, *5*, 4254–4279.

[5] Li, Q.; Dang, R. B.; Chen, M. M.; Lee, Y. L.; Hu, Z. B.; Xiao, X. L. Synthesis method for long cycle life lithium-ion cathode material: Nickel-rich core-shell $LiNi_{0.8}Co_{0.1}Mn_{0.1}O_2$. *ACS Appl. Mater. Interfaces* **2018**, *10*, 17850–17860.

[6] Nan, C. Y.; Lu, J.; Li, L. H.; Li, L. L.; Peng, Q.; Li, Y. D. Size and shape control of $LiFePO_4$ nanocrystals for better lithium ion battery cathode materials. *Nano Res.* **2013**, *6*, 469–477.

[7] Zhao, S. Q.; Yan, K.; Zhang, J. Q.; Sun, B.; Wang, G. Q. Enhanced electrochemical performance in lithium ion batteries of a hollow spherical lithium-rich cathode material synthesized by a molten salt method. *Angew. Chem., Int. Ed.* **2020**, *6*, 2208–2210.

[8] Boulineau, A.; Croguennec, L.; Delmas, C.; Weill, F. Reinvestigation of Li_2MnO_3 structure: Electron diffraction and high resolution TEM. *Chem. Mater.* **2009**, *21*, 4216–4222.

[9] Zhu, W.; Tai, Z. G.; Shu, C. Y.; Chong, S. K.; Guo, S. W.; Ji, L. J.;

Chen, Y. Z.; Liu, Y. N. The superior electrochemical performance of a Li-rich layered cathode material with Li-rich spinel $Li_4Mn_5O_{12}$ and MgF_2 double surface modifications. *J. Mater. Chem. A* **2020**, *8*, 7991–8001.

[10] Zhang, L. J.; Wu, B. R.; Li, N.; Wu, F. Hierarchically porous micro-rod lithium-rich cathode material $Li_{1.2}Ni_{0.13}Mn_{0.54}Co_{0.13}O_2$ for high performance lithium-ion batteries. *Electrochim. Acta* **2014**, *118*, 67–74.

[11] Zhang, Y.; Zhang, W. S.; Shen, S. Y.; Yan, X. H.; Wu, A. M.; Yin, J. W.; Zhang, J. L. Hollow porous bowl-shaped lithium-rich cathode material for lithium-ion batteries with exceptional rate capability and stability. *J. Power Sources* **2018**, *380*, 164–173.

[12] Liu, Y. C.; Wang, J.; Wu, J. W.; Ding, Z. Y.; Yao, P. H.; Zhang, S. L.; Chen, Y. N. 3D cube-maze-like Li-rich layered cathodes assembled from 2D porous nanosheets for enhanced cycle stability and rate capability of lithium-ion batteries. *Adv. Energy Mater.* **2020**, *10*, 1903139.

[13] Wang, Z.; Lin, X. Y.; Zhang, J. T.; Wang, D.; Ding, C. Y.; Zhu, Y. M.; Gao, P.; Huang, X. X.; Wen, G. W. Spherical layered Li-rich cathode material: Unraveling the role of oxygen vacancies on improving lithium ion conductivity. *J. Power Sources* **2020**, *462*, 228171.

[14] He, Z. J.; Wang, Z. X.; Huang, Z. M.; Chen, H.; Li, X. H.; Guo, H. J. A novel architecture designed for lithium rich layered $Li[Li_{0.2}Mn_{0.54}Ni_{0.13}Co_{0.13}]O_2$ oxides for lithium-ion batteries. *J. Mater. Chem. A* **2015**, *3*, 16817–16823.

[15] Li, Y.; Bai, Y.; Wu, C.; Ji, Q.; Chen, G. H.; Liu, L.; Wang, H.; Zhou, X. Z.; Wu, F. Three-dimensional fusiform hierarchical micro/nano $Li_{1.2}Ni_{0.2}Mn_{0.6}O_2$ with a preferred orientation (110) plane as a high energy cathode material for lithium-ion batteries. *J. Mater. Chem. A* **2016**, *4*, 5942–5951.

[16] de Biasi, L.; Schwarz, B.; Brezesinski, T.; Hartmann, P.; Janek, J.; Ehrenberg, H. Chemical, structural, and electronic aspects of formation and degradation behavior on different length scales of Ni-Rich NCM and Li-Rich HE-NCM cathode materials in Li-ion batteries. *Adv. Mater.* **2019**, *31*, 1900985.

[17] Gent, W. E.; Li, Y. Y.; Ahn, S.; Lim, J.; Liu, Y. J.; Wise, A. M.; Gopal, C. B.; Mueller, D. N.; Davis, R.; Weker, J. N. et al. Persistent state-of-charge heterogeneity in relaxed, partially charged $Li_{1-x}Ni_{1/3}Co_{1/3}Mn_{1/3}O_2$ secondary particles. *Adv. Mater.* **2016**, *28*, 6631−6638.

[18] Lei, Y. K.; Ni, J.; Hu, Z. J.; Wang, Z. M.; Gui, F. K.; Li, B.; Ming, P. W.; Zhang, C. M.; Elias, Y.; Aurbach, D. et al. Surface modification of Li-rich Mn-based layered oxide cathodes: Challenges, materials, methods, and characterization. *Adv. Energy Mater.* **2020**, *10*, 2002506.

[19] Zhang, X.; Zhou, Y, P.; Luo, B.; Zhu, H. C.; Chu, W.; Huang, K. Microwave-assisted synthesis of $NiCo_2O_4$ double-shelled hollow spheres for high-performance sodium ion batteries. *Nano-Micro Lett.* **2018**, *10*, 13.

[20] Yu, X. Y.; Yao, X. Z.; Luo, T.; Jia, Y.; Liu, J. H.; Huang, X. J. Facile synthesis of urchin-like $NiCo_2O_4$ hollow microspheres with enhanced electrochemical properties in energy and environmentally related applications. *ACS Appl. Mater. Interfaces* **2014**, *6*, 3689–3695.

[21] Li, Y. X.; Mei, J.; Guo, X. D.; Zhong, B. H.; Liu, H.; Liu, G. B.; Dou, S. X. Hollow $Li_{1.2}Mn_{0.54}Ni_{0.13}Co_{0.13}O_2$ micro-spheres synthesized by a co-precipitation method as a high-performance cathode material for Li-ion batteries. *RSC Adv.* **2016**, *6*, 70091–70098.

[22] He, X.; Wang, J.; Kloepsch, R.; Krueger, S.; Jia, H. P.; Liu, H. D.; Vortmann, B.; Jie, L. Enhanced electrochemical performance in lithium ion batteries of a hollow spherical lithium-rich cathode material synthesized by a molten salt method. *Nano Res.* **2014**, *7*, 110–118.

[23] Liu, X. P.; Gong, M. X.; Deng, S. F.; Zhao, T. H.; Zhang, J.; Wang, D. L. Recent advances on metal alkoxide-based electrocatalysts for water splitting. *J. Mater. Chem. A* **2020**, *8*, 10130–10149.

[24] Shen, L. F.; Yu, L.; Yu, X. Y.; Zhang X. G.; Lou, X. W. Self-templated formation of uniform $NiCo_2O_4$ hollow spheres with complex interior structures for lithium-ion batteries and supercapacitors. *Angew. Chem., Int. Ed.* **2015**, *127*, 1888–1892.

[25] Zhang, G. Q.; Lou, X. W. General synthesis of multi-shelled mixed metal oxide hollow spheres with superior lithium storage properties. *Angew. Chem.* **2014**, *126*, 9187–9190.

[26] Yu, F. D.; Que, L. F.; Wang, Z. B.; Zhang, Y.; Xue, Y.; Liu, B. S.; Gu, D. M. Layered-spinel capped nanotube assembled 3D Li-rich hierarchitectures for high performance Li-ion battery cathodes. *J. Mater. Chem. A* **2016**, *4*, 18416–18425.

[27] Zi, Z. Y.; Zhang, Y. T.; Meng, Y. Q.; Gao, G.; Hou, P. Y. Hierarchical Li-rich oxide microspheres assembled from {010} exposed primary grains for high-rate lithium-ion batteries. *New J. Chem.* **2020**, *44*, 8486–8493.

[28] Kim, J. H.; Kang, Y. C. Yolk-shell-structured $(Fe_{0.5}Ni_{0.5})_9S_8$ solid-solution powders: Synthesis and application as anode materials for Na-ion batteries. *Nano Res.* **2017**, *10*, 3178–3188.

[29] Li, H. L.; Ren, Y. B.; Yang, P. H.; Jian, Z. X.; Wang, W. X.; Xing, Y. L.; Zhang, S. C. Morphology and size controlled synthesis of the hierarchical structured $Li_{1.2}Mn_{0.54}Ni_{0.13}Co_{0.13}O_2$ cathode materials for lithium ion batteries. *Electrochim. Acta* **2019**, *297*, 406–416.

[30] Xu, M.; Fei, L. F.; Zhang, W. B.; Li, T.; Lu, W.; Zhang, N.; Lai, Y. Q.; Zhang, Z. A.; Fang, J.; Zhang, K. et al. Tailoring anisotropic Li-ion transport tunnels on orthogonally arranged Li-rich layered oxide nanoplates toward high-performance Li-ion batteries. *Nano Lett.* **2017**, *17*, 1670–1677.

[31] Guo, F. F.; Fan, M. H.; Jin, P. P.; Chen, H.; Wu, Y. Y.; Li, G. D.; Zou, X. X. Precursor-mediated synthesis of double-shelled V_2O_5 hollow nanospheres as cathode material for lithium-ion batteries. *CrystEngComm* **2016**, *18*, 4068–4073.

[32] Nayak, P. K.; Erickson, E. M.; Schipper, F.; Penki, T. R.; Munichandraiah, N.; Adelhelm, P.; Sclar, H.; Amalraj, F.; Markovsky; B.; Aurbach, D. Review on challenges and recent advances in the electrochemical performance of high capacity Li- and Mn-rich cathode materials for Li-Ion batteries. *Adv. Energy Mater.* **2018**, *8*, 1702397.

[33] Wu, K.; Li, Q.; Dang, R. B.; Deng, X.; Chen, M. M.; Lee, Y. L.; Xiao, X. L.; Hu, Z. B. A novel synthesis strategy to improve cycle stability of $LiNi_{0.8}Mn_{0.1}Co_{0.1}O_2$ at high cut-off voltages through core-shell structuring. *Nano Res.* **2019**, *12*, 2460–2467.

[34] Amine, K.; Tukamoto, H.; Yasuda, H.; Fujita, Y. A new three-volt spinel $Li_{1+x}Mn_{1.5}Ni_{0.5}O_4$ for secondary lithium batteries. *J. Electrochem. Soc.* **1996**, *143*, 1607–1613.

[35] Hu, W. H.; Zhang, Y. X.; Zan, L.; Cong, H. J. Mitigation of voltage decay in Li-rich layered oxides as cathode materials for lithium-ion batteries. *Nano Res.* **2020**, *13*, 151–159.

[36] Li, H. Practical evaluation of Li-ion batteries. *Joule* **2019**, *3*, 911–914.

[37] Ma, Y. T.; Liu, P. F.; Xie, Q. S.; Zhang, G. B.; Zheng, H. F.; Cai, Y. X.; Li, Z.; Wang, L. S.; Zhu, Z. Z.; Mai, L. Q. et al. Double-shell Li-rich layered oxide hollow microspheres with sandwich-like carbon@spinel@layered@spinel@carbon shells as high-rate lithium ion battery cathode. *Nano Energy* **2019**, *59*, 184–196.

[38] Li, L. Y.; Liu, Y. C.; Yu, H. B.; Sun, R. T.; Ding, Z. Y.; Li, K. K.; Yuan, Q. H.; Wu, J. W.; Liu, X. J. Hollow spherical $0.5Li_2MnO_3{\cdot}0.5LiMn_{1/3}Ni_{1/3}Co_{1/3}O_2$ prepared by facile molten salt method for enhanced long-cycle and rate capability of lithium-ion batteries. *J. Alloys Compd.* **2021**, *855*, 157376.

[39] Shi, S. J.; Lou, Z. R.; Xia, T. F.; Wang, X. L.; Gu, C. D.; Tu, J. P. Hollow $Li_{1.2}Mn_{0.5}Co_{0.25}Ni_{0.05}O_2$ microcube prepared by binary template as a cathode material for lithium ion batteries. *J. Power Sources* **2014**, *257*, 198–204.

[40] Lou, M.; Zhong, H.; Yu, H. T.; Fan, S. S.; Xie, Y.; Yi, T. F. $Li_{1.2}Mn_{0.54}Ni_{0.13}Co_{0.13}O_2$ hollow hierarchical microspheres with enhanced electrochemical performances as cathode material for lithium-ion battery application. *Electrochim. Acta* **2017**, *237*, 217–226.

[41] Yu, X. Q.; Lyu, Y. C.; Gu, L.; Wu, H. M.; Bak, S. M.; Zhou, Y. N.; Amine, K.; Ehrlich, S. N.; Li, H.; Nam, K. W. et al. Understanding the rate capability of high-energy-density Li-rich layered $Li_{1.2}Ni_{0.15}Co_{0.1}Mn_{0.55}O_2$ cathode materials. *Adv. Energy Mater.* **2014**, *4*, 1300950.

[42] Heubner, C.; Schneider, M.; Michaelis, A. Heat generation rates of $NaFePO_4$ electrodes for sodium-ion batteries and $LiFePO_4$ electrodes

for lithium-ion batteries: A comparative study. *J. Solid State Electrochem.* **2018**, *22*, 1099–1108.

[43] Sun, J. P.; Tang, K.; Yu, X. Q.; Hu, J.; Li, H.; Huang, X. J. Overpotential and electrochemical impedance analysis on Cr_2O_3 thin film and powder electrode in rechargeable lithium batteries. *Solid State Ionics* **2008**, *179*, 2390–2395.

[44] Zheng, J. M.; Shi, W.; Gu, M.; Xiao, J.; Zuo, P. J.; Wang, C. M.; Zhang, J-G. Electrochemical kinetics and performance of performance of layered composite cathode material $Li[Li_{0.2}Ni_{0.2}Mn_{0.6}]O_2$. *J. Electrochem. Soc.* **2013**, *160*, A2212–A2219.

[45] Yu, F. D.; Que, L. F.; Wang, Z. B.; Xue, Y.; Zhang, Y.; Liu, B. S.; Gu, D. M. Controllable synthesis of hierarchical ball-in-ball hollow microspheres for a high performance layered Li-rich oxide cathode material. *J. Mater. Chem. A* **2017**, *5*, 9365–9376.

[46] Ding, W. X.; Cui, X. Y.; Lei, J.; Lin, X. D.; Zhao, S. L.; Wu, Q. H.; Zheng, M. S.; Dong, Q. F. Hollow spherical lithium-rich layered oxide cathode material with suppressed voltage fading. *Electrochim. Acta* **2018**, *264*, 260–268.

[47] Xu, X.; Huo, H.; Jian, J. Y.; Wang, L. G.; Zhu, H.; Xu, S.; He, X. S.; Yin, G. P.; Du, C. Y.; Sun, X. L. Radially oriented single-crystal primary nanosheets enable ultrahigh rate and cycling properties of $LiNi_{0.8}Co_{0.1}Mn_{0.1}O_2$ cathode material for lithium-ion batteries. *Adv. Energy Mater.* **2019**, *9*, 1803963.

[48] Kondrakov, A. O.; Schmidt, A.; Xu, J.; Geßwein, H.; Mönig, R.; Hartmann, P.; Sommer, H.; Brezesinski, T.; Janek, J. Anisotropic lattice strain and mechanical degradation of high- and low-nickel NCM cathode materials for Li-ion batteries. *J. Phys. Chem. C* **2017**, *121*, 3286–3294.

[49] Zhang, K.; Li, B.; Zuo, Y. X.; Song, J.; Shang, H. F.; Ning, F. H.; Xia, D. G. Voltage decay in layered Li-rich Mn-based cathode materials. *Electrochem. Energy Rev.* **2019**, *2*, 606–623.

[50] Yan, P. F.; Zheng, J. M.; Gu, M.; Xiao, J.; Zhang, J. G.; Wang, C. M. Intragranular cracking as a critical barrier for high-voltage usage of layer-structured cathode for lithium-ion batteries. *Nat. Commun.* **2017**, *8*, 14101.

[51] Zheng, J. M.; Gu, M.; Xiao, J.; Zuo, P. J.; Wang, C. M.; Zhang, J. G. Corrosion/fragmentation of layered composite cathode and related capacity/voltage fading during cycling process. *Nano Lett.* **2013**, *13*, 3824–3830.

[52] Qian, D. N.; Xu, B.; Chi, M. F.; Meng, Y. S. Uncovering the roles of oxygen vacancies in cation migration in lithium excess layered oxides. *Phys. Chem. Chem. Phys.* **2014**, *16*, 14665–14668.

[53] Hu, E. Y.; Yu, X. Q.; Lin, R. Q.; Bi, X. X.; Lu, J.; Bak, S.; Nam, K. W.; Xin, H. L.; Jaye, C.; Fischer, D. A. et al. Evolution of redox couples in Li- and Mn-rich cathode materials and mitigation of voltage fade by reducing oxygen release. *Nat. Energy* **2018**, *3*, 690–698.

[54] Yang, W. L. Oxygen release and oxygen redox. *Nat. Energy* **2018**, *3*, 619–620.

[55] Sun, G.; Yu, F. D.; Que, L. F.; Deng, L.; Wang, M. J.; Jiang, Y. S.; Shao, G. J.; Wang, Z. B. Local electronic structure modulation enhances operating voltage in Li-rich cathodes. *Nano Energy* **2019**, *66*, 104102.

[56] Liu, S.; Liu, Z. P.; Shen, X.; Li, W. H.; Gao, Y. R.; Banis, M. N.; Li, M. S.; Chen, K.; Zhu, L.; Yu, R. C. et al. Surface doping to enhance structural integrity and performance of Li-rich layered oxide. *Adv. Energy Mater.* **2018**, *8*, 1802105.